


Article

Catalytic Effect of Hydrogen Bond on Oxhydryl Dehydrogenation in Methanol Steam Reforming on Ni(111)

Changming Ke ¹ and Zijing Lin ^{2,*} 

¹ Hefei National Laboratory for Physical Sciences at Microscales, Department of Physics, School of Physical Sciences, University of Science and Technology of China, Hefei 230052, Anhui, China; cmk@mail.ustc.edu.cn

² CAS Key Laboratory of Strongly-Coupled Quantum Matter Physics, Department of Physics, School of Physical Sciences, University of Science and Technology of China, Hefei 230052, Anhui, China

* Correspondence: zjlin@ustc.edu.cn; Tel.: +86-551-63606345; Fax: +86-551-63606348

Received: 19 December 2019; Accepted: 25 March 2020; Published: 27 March 2020



Abstract: Dehydrogenation of H₃COH and H₂O are key steps of methanol steam reforming on transition metal surfaces. Oxhydryl dehydrogenation reactions of H_xCOH ($x = 0-3$) and OH on Ni (111) were investigated by DFT calculations with the OptB88-vdW functional. The transition states were searched by the climbing image nudged elastic band method and the dimer method. The activation energies for the dehydrogenation of individual H_xCOH* are 68 to 91 kJ/mol, and reduced to 12–17 kJ/mol by neighboring OH*. Bader charge analysis showed the catalysis role of OH* can be attributed to the effect of hydrogen bond (H-bond) in maintaining the charge of oxhydryl H in the reaction path. The mechanism of H-bond catalysis was further demonstrated by the study of OH* and N* assisted dehydrogenation of OH*. Due to the universality of H-bond, the H-bond catalysis shown here, is of broad implication for studies of reaction kinetics.

Keywords: Reaction mechanism; first-principle calculation; Bader charge analysis; activation energy; transition state structure

1. Introduction

Methanol steam reforming (MSR), $\text{H}_3\text{COH} + \text{H}_2\text{O} \rightarrow \text{CO}_2 + 3\text{H}_2$, is frequently used for the generation of H₂ at temperatures of 200–300 °C and atmospheric pressure [1–4]. MSR can be catalysed by a number of metals and metal oxides. Cu is the most common commercial catalyst but suffers from pyrophoricity and catalyst sintering, limiting its long-term applications [5,6]. Noble metals, such as Pd and Pt, that possess long term stability and no pyrophoric behavior [3,7] suffer from high price, limiting their large-scale industrial applications. On balance, Ni is a low price and highly effective MSR catalyst. The high activity of Ni for catalyzing MSR at $T \geq 300^\circ\text{C}$ has been demonstrated in recent experiments [5,6], but a convincing theoretical explanation of the reaction mechanism is lacking.

There have been numerous theoretical studies on the reaction mechanism of MSR over a number of catalysts. Lin et al. conducted density functional theory (DFT) calculations and built a kinetic model of MSR on Cu(111) [8]. They found kinetic relevant steps with high activation energies include $\text{H}_3\text{COH}^* + * \rightarrow \text{H}_3\text{CO}^* + \text{H}^*$ and, where * denotes an active surface site and R* means a surface adsorbed species R. Zuo et al. discussed the mechanisms of methanol decomposition, methanol oxidation and steam reforming of methanol on Cu(111) [9]. Wang et al. explained the differentiation of intrinsic reactivity of MSR on Cu, CuZn and Cu/ZnO [10]. In addition, they proposed a microkinetic model for more in-depth mechanics research of MSR on Cu [11]. Smith et al. conducted DFT studies on the initial steps of MSR on PdZn and ZnO surfaces, and found defect sites lower the barrier significantly [12]. Also based on DFT calculations, Krajčí et al. demonstrated the CO/CO₂ selectivity of MSR on many alloys,

e.g., PdZn, PtZn and NiZn [13]. Chen et al. [14], Lausche et al. [15], and Kramer et al. [16] studied the selectivity of the dehydrogenation of methanol on Cu(110), Ni(100) and Ni(111), respectively. MSRs on Pt [16], Pd [16], Pt₃Ni alloy [17], Pt-Skinned PtNi Bimetallic Clusters [18] and Co [19] have also been investigated.

Summarizing the existing results of MSR studies, there are two kinds of MSR kinetics. The first was deduced by considering the dehydrogenation of isolate adsorbed H_xCOH ($x = 3, 2, 1, 0$). As the activation energy for the bond breaking of H₃CO-H* is high, H₃COH* + * → H₃CO* + H* was found to be a likely rate determining step (RDS) [8,10,11,17]. For example, Wang et al. [11] showed in their DFT study that the activation energy for CH₃OH* + * → CH₃O* + H* was 103 kJ/mol and MSR on Cu(111) was mostly limited by the dehydrogenation of CH₃OH*. The second considered the interaction of H₃COH* and OH* where the co-adsorbed OH* significantly reduces the activation energy of H₃COH* + OH* → H₃CO* + H₂O* and the C–H scission steps were found to be rate limiting [9,13,19]. The resulting kinetics with a lower activation energy agrees better with the experiments [20,21], and is a clear improvement of the first one. Unfortunately, the improved understanding has so far been mainly limited to a computational detail based deduction. In-depth understanding based on general physical concept and/or generable mechanism is highly desirable.

This work focuses on the role of hydrogen bond (H-bond) on reducing the activation energies of oxhydryl dehydrogenation that are important for determining the kinetics of MSR on Ni(111), the dominant catalyzing surface of micron-sized commercial Ni catalysts [22]. DFT calculations were performed to examine the oxhydryl dehydrogenation of H_xCO–H* ($x = 3, 2, 1, 0$), with and without the assistance of the co-adsorbed OH*. Combined analysis of Bader charges and transition state structures showed that H-bond is the root cause for the observed high MSR activity. The catalytic role of H-bond was further supported by investigating the dehydrogenation of O–H* assisted by co-adsorbed N*.

2. Computational Methods

DFT calculations were performed using Vienna Ab-initio Simulation Package (VASP) [23–26], a plane wave computational software. The projector augmented wave (PAW) method [27,28] was used to describe the electron-ion interaction between core ion and valence electrons. The Kohn-Sham equations were solved with a 380eV cutoff energy for the wavefunctions of valence electrons. The exchange correlation interaction was described by the functional of OptB88-vdW [29,30]. OptB88-vdW was chosen as it best describes the van der Waals (vdW) interaction on metal surface [31]. The computations were performed on a three-layer slab of 3 × 3 unit cell surface model of Ni(111), with a vacuum region of 10 Å thickness. The surface layer of the slab was allowed to relax, while the bottom two layers were fixed. Spin polarization and dipole correction were considered by setting SPIN = 2 and LDIPOL = .True in all calculations. The Brillouin zone was sampled by a 5 × 5 × 1 k-point Monkhorst-Pack grid. All stable structures were optimized with an energy-based conjugate gradient algorithm [32]. The convergence criteria for electronic and ionic energies were 10^{−6} eV/atom and 10^{−5} eV/atom, respectively. The cutoff energy and the k-point grid were tested to be appropriate, e.g., the differences in the obtained adsorption energy of H₃CO are less than 0.4 kJ/mol and 0.7 kJ/mol when compared to a cutoff energy of up to 460 eV and a k-point grid of up to 8 × 8 × 1, respectively.

Saddle points were determined by combining the climbing image nudged elastic band (CL-NEB) method [33] and the dimer method [34]. First, the less computing intensive CL-NEB was used to find the minimum energy path and the transition state. In the CL-NEB calculations, 7 images were inserted between reactants and products, and the electronic energies and the forces were converged to 10^{−4} eV/atom and 0.03 eV/Å, respectively. Second, the transition states obtained by the CL-NEB searches were used as the inputs for the high-precision dimer method [34] to find the accurate transition states efficiently. In the dimer method calculations, the electronic energy and force were converged respectively to 10^{−7} eV/atom and 0.01 eV/Å.

The Bader charge was calculated by the method of partitioning charge density grids into Bader volumes, as proposed by Henkelman's group [35,36].

3. Results and Discussion

3.1. Oxhydryl Dehydrogenation of H_xCOH^*

Oxhydryl dehydrogenation of isolated H_xCOH^* ($x = 3, 2, 1, 0$), $H_xCOH^* + * \rightarrow H_xCO^* + H^*$, and that assisted by co-adsorbed OH, $H_xCOH^* + OH^* \rightarrow H_xCO^* + H_2O^*$, were considered. The activation barriers of the two types of dehydrogenation reactions were compared in Figure 1.

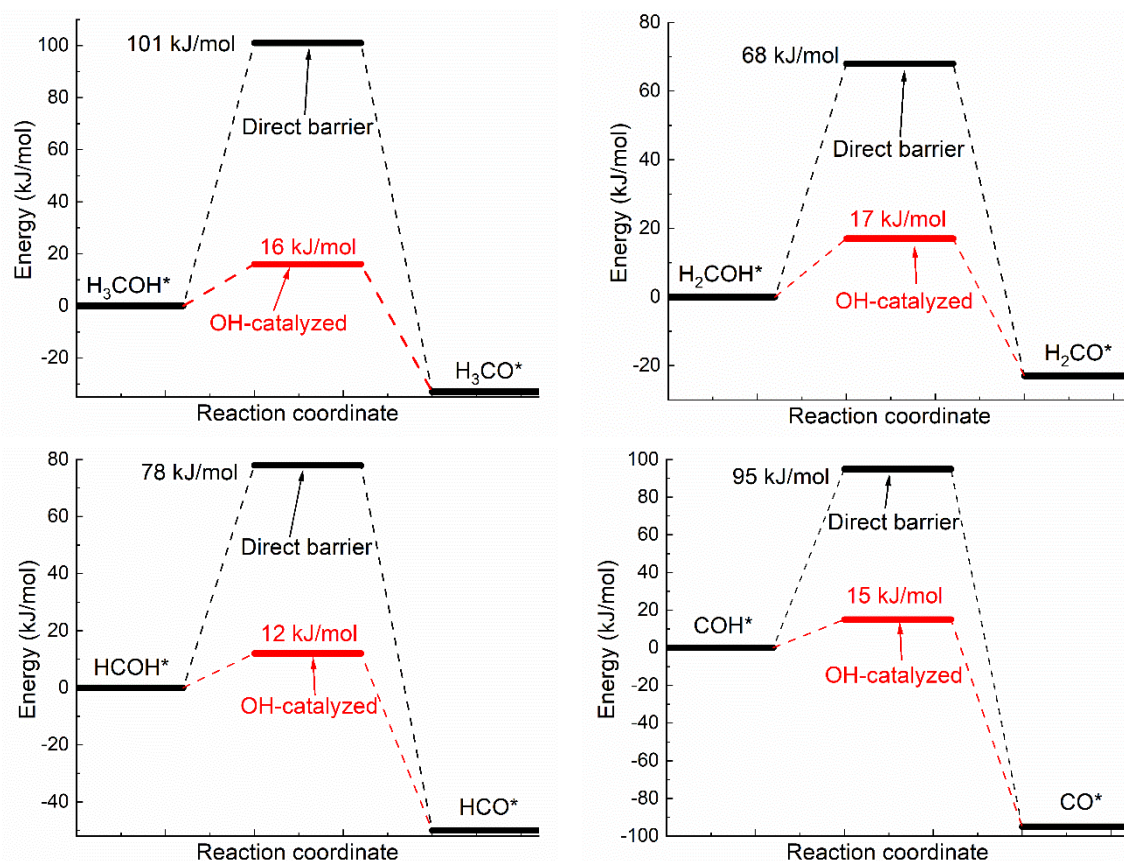


Figure 1. Activation energies of dual path dehydrogenation of oxhydryl in H_xCO-H^* ($x = 3, 2, 1, 0$).

Notice that the direct barrier of H_3COH^* dehydrogenation shown Figure 1 is about 91 kJ/mol. In comparison, the barrier was found to range from 39 to 75 kJ/mol in a few early studies [16,37,38]. The difference, due to various factors such as the use of different functionals, surface slab model and transition state search methods, is quite substantial, but is also seen in similar cases. For example, the direct barrier of H_3COH^* dehydrogenation on Cu(111) was found to vary from 62 to 138 kJ/mol by different DFT studies [8–11,39]. That is, the difference known for Cu(111) is comparable to that known for Ni(111). Although it is premature to draw any conclusion, the result here may be preferable due to the demonstrated quality of OptB88-vdW for similar systems [31] and the widely accepted slab model and transition state search method.

As shown in Figure 1, the activation energies (E_a 's) of oxhydryl dehydrogenation of H_xCOH^* are reduced from 68–91 kJ/mol for isolated H_xCOH^* to 12–17 kJ/mol for H_xCOH^* with co-adsorbed OH ($x = 3, 2, 1, 0$). The reduction of E_a for the oxhydryl dehydrogenation of H_3COH^* due to the presence of neighboring OH* is known in literatures. For example, E_a is reduced from 62 kJ/mol to 32 kJ/mol for Cu(111) [9] and from 80 kJ/mol to 22 kJ/mol for Co(111) [19]. The results here concerning the oxhydryl dehydrogenation of H_xCOH^* for $x = 2, 1, 0$ indicate that the effect is quite general. The low activation energies mean that all oxhydryl dehydrogenation processes of H_xCOH^* in MSR should be sufficiently fast. Besides, the energy cost for a close proximity of H_xCOH^* and OH* as compared to

isolated adsorbates is low, at 7.7, 14, 11, 5.1 kJ/mol for $x = 3, 2, 1, 0$, respectively. Therefore, there is no need to consider the oxhydryl dehydrogenation processes of H_xCOH^* when examining the possible RDS in MSR. This result can be used to simplify the elementary reaction step study in many relevant problems. A low E_a for H_3COH^* dehydrogenation is also necessary for the understanding of the high MSR activities of Ni catalysts observed experimentally [5,6].

Notice that, while OH^* facilitates the O–H scission process, OH^* provides no help for C–H scission. The activation energies for $CH_3O^* + OH^* \rightarrow CH_2O^* + H_2O^*$ and $CH_3OH^* + OH^* \rightarrow CH_2OH^* + H_2O^*$ are 166 and 149 kJ/mol, respectively. Both the activation energies are higher than the corresponding activation energies of 86.8 and 91.5 kJ/mol for $CH_3O^* \rightarrow CH_2O^* + H^*$ and $CH_3OH^* \rightarrow CH_2OH^* + H^*$, respectively. Similar result has also been observed for the C–H scission on PdZn(111) [40]. As reactions prefer the least resistant paths and the fractional coverage of OH^* is in the order of 1% and very low coverages for CH_3OH^* and CH_xO^* on Ni(111) [41], the C–H scission is not expected to be adversely impacted by OH^* . Due to the high E_a involved in $CH_3O^* \rightarrow CH_2O^* + H^*$ or $CH_3OH^* \rightarrow CH_2OH^* + H^*$. However, the C–H scission step is expected to be rate limiting for MSR on Ni(111).

To reveal the common feature of oxhydryl dehydrogenation in different H_xCOH^* , Figure 2 shows the structures and Bader charges of H_xCOH^* , with and without OH^* co-adsorption, at their initial local minimum geometries and reaction transition states. As seen in Figure 2, the Bader charges of oxhydryl H for isolated H_xCOH^* at their local minimum and transition state structures are on average +0.63 e and +0.14 e, respectively. Clearly, the Bader charges of oxhydryl H of isolated H_xCOH^* at their local minimum and transition state structures are quite different. That is, a significant charge density redistribution is required in the reaction path going from a local minimum energy structure to a transition state configuration. A large electronic energy changes due to the orbital reorganization, or correspondingly a high energy barrier, is expected in the O–H scission process. In comparison, the Bader charges for oxhydryl H of H_xCOH^* with co-adsorbed OH^* are on average +0.59 e and +0.65 e at the minimum energy and transition state structures, respectively. There are little charge redistributions required in the bond scission reaction paths. Combined with the fact that the O–H bond of H_xCOH^* is floppy, a very low activation energy is encountered for each of the reactions.

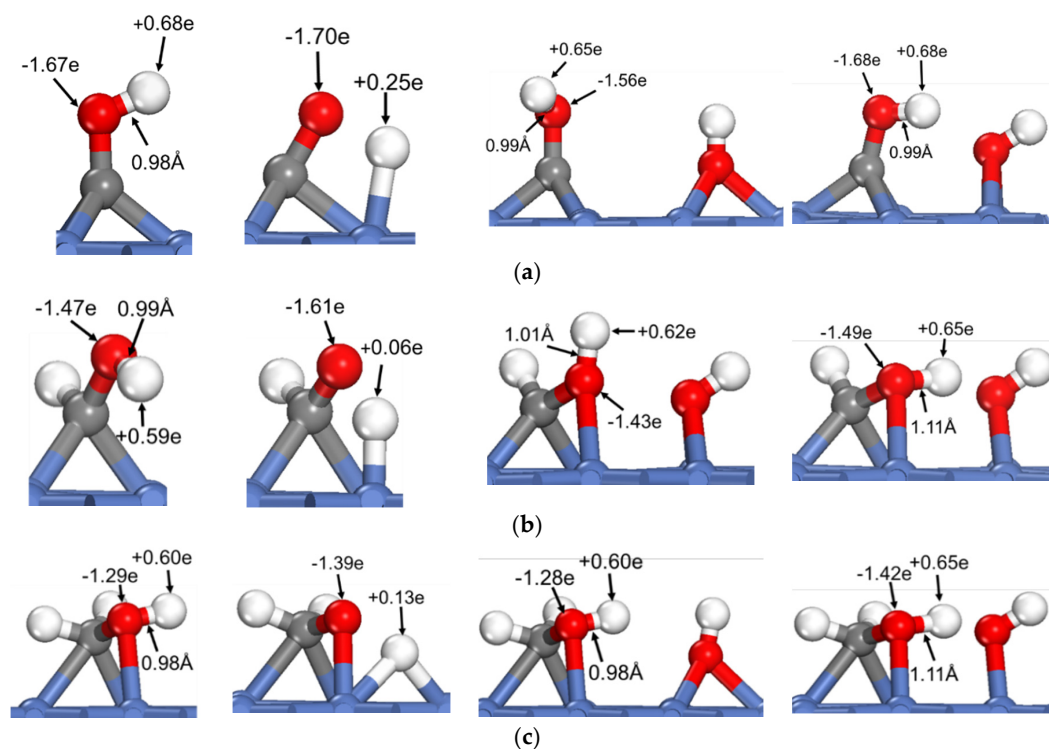


Figure 2. Cont.

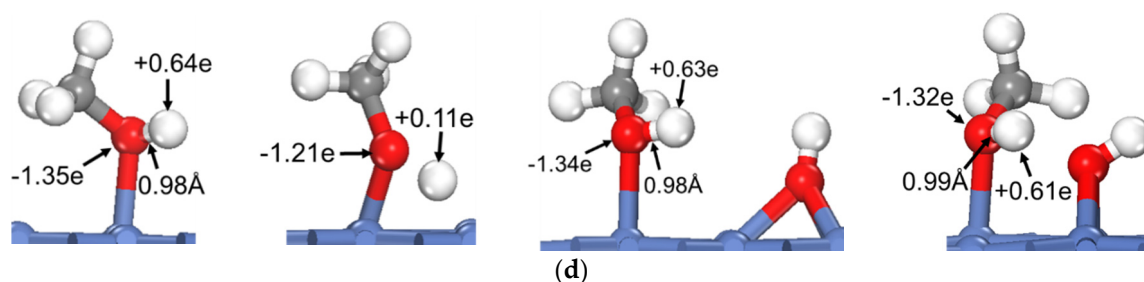


Figure 2. Structures and Bader charges in the oxhydryl dehydrogenation of H_xCOH with and without co-adsorbed OH: (a) $x = 0$, (b) $x = 1$, (c) $x = 2$, (d) $x = 3$. From left to right: local minimum and transition state structures of H_xCOH without and with co-adsorbed OH.

Based on the above analysis, it is clear that OH^* plays a catalyzing role in the oxhydryl dehydrogenation of H_xCOH^* on Ni(111). The catalysis effect is realized by minimizing the charge redistribution requirement in the reaction path. The charge of oxhydryl H of H_xCOH^* in the reaction process is maintained by interacting with OH^* . The $H \cdots OH$ distance at the transition structure is 1.86, 1.61, 1.67 and 2.05 Å for $x = 0, 1, 2$, and 3, respectively. The distances are characteristics of H-bonds. Therefore, the reduced reaction barrier for the oxhydryl dehydrogenation of H_xCOH^* can be attributed to the catalyzing effect of H-bond interaction.

3.2. Dehydrogenation of OH^* Assisted by H-Bond of $O-H \cdots OH$ and $O-H \cdots N$

The catalyzing effect of H-bond on oxhydryl dehydrogenation can also be seen in the dehydrogenation of OH^* adsorbed on Ni(111) [42]. Figure 3 compares the activation energies, initial and transition state structures and charge distributions of OH^* dehydrogenations with and without co-adsorbed neighboring OH^* . As seen in Figure 3, the activation energy of dehydrogenation is 105 kJ/mol for isolated OH^* , but is reduced by 37 kJ/mol to 68 kJ/mol for OH^* with co-adsorbed OH^* due to the $O-H \cdots OH$ interaction. The reduction of activation energy is also observed for other transition metals. The activation energy for the corresponding reaction is reduced from 1.11 eV to 0.3 eV on Co(111) [19] and from 1.88 eV to 0.82 eV on Cu(111) [9]. Moreover, the higher energy of $O^* + H_2O^*$ in comparison with that of $OH^* + OH^*$ is in qualitative agreement with both the theoretical and experimental results of Che et al [43].

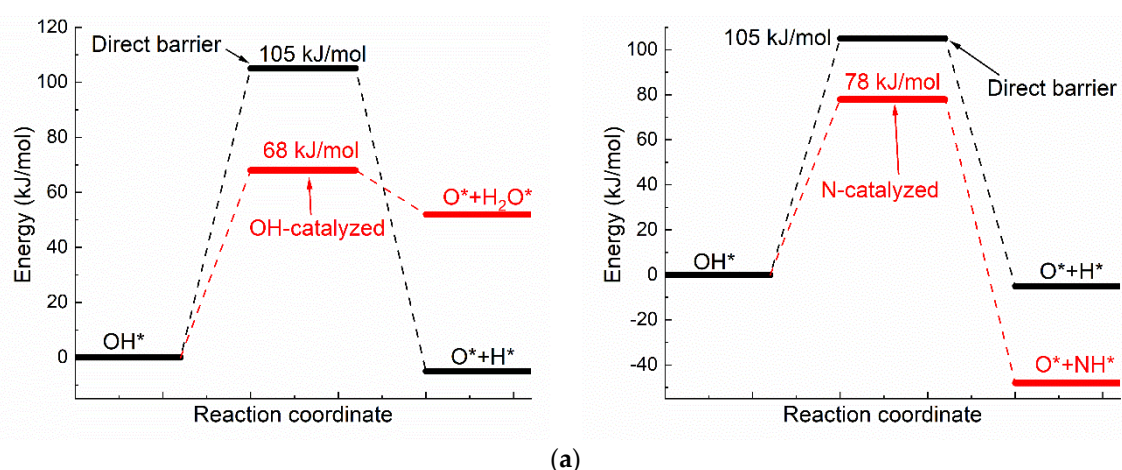


Figure 3. Cont.

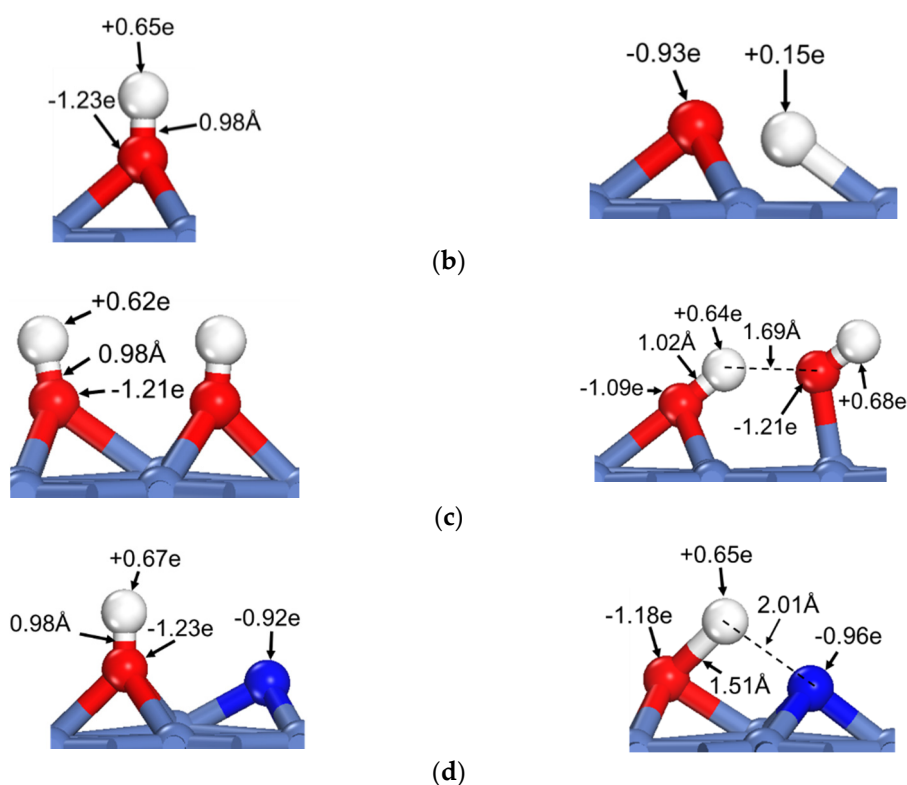


Figure 3. The dehydrogenation of O–H on Ni(111) surface: (a) The activation energies of dual path dehydrogenation of OH*, (b) The initial and transition state structures and charge distributions of individual OH* dehydrogenation, (c) The initial and transition state structures and charge distributions of OH-catalyzed OH* dehydrogenation, (d) The initial and transition state structures and charge distributions of N-catalyzed OH* dehydrogenation.

Like the case shown in Figure 2, the Bader charges of H for the energy minimum and transition state structures in the dehydrogenation of individual OH* are quite different, at +0.65e and +0.15e, respectively. The corresponding Bader charges are respectively +0.62e and +0.64e in the dehydrogenation of OH* with the presence of the O–H···OH interaction. Once again, the charge of oxyhydril H remains almost constant in the reaction process due to the influence of the O–H···OH H-bond.

H-bonds are ubiquitous in nature and normally exist between electronegative atoms and H atoms covalently bound to similar electronegative atoms. In addition to the OH···O H-bond discussed above, OH···N is another type of commonly seen H-bond. Even though OH···N is not involved in MSR, it may exist in other reaction processes. To test the conceptual generality of H-bond catalysis, the effect of OH···N H-bond on OH* dehydrogenation is examined here.

The activation energy, initial and transition state structures and charge distributions of OH* dehydrogenations with neighboring N* are also shown in Figure 3. As shown in Figure 3, the activation energy of OH* dehydrogenation is reduced by 27 kJ/mol due to the presence of OH···N interaction. Like the cases shown for OH···O interactions, the charge of oxyhydril H changes little in going from the initial local minimum structure to the transition state, even though the direction and distance of the O–H bond are substantially changed in the process.

Combining Figures 2 and 3, a general conclusion may be drawn: the charge of oxyhydril H is kept unchanged in the initial and transition states of dehydrogenation by the presence of H-bond. As a result, the activation energy for the dehydrogenation reaction is reduced in comparison to that in the absence of the H-bond.

It is worth noting that the activation energy is reduced to a very low value of around 15 kJ/mol, for the dehydrogenation of H_xCOH^* , but to 68–78 kJ/mol for the OH^* dehydrogenation. The notable difference is attributable to the rigidity of the O–H bond in the species: The O–H bond directionality is quite weak in H_xCOH^* , while relatively strong in OH^* . Another point to note is that the activation energy for the $H \cdots N$ assisted reaction is 10 kJ/mol higher than that of $H \cdots O$ assisted process, even though the $H \cdots N$ interaction is known to be stronger than the $H \cdots O$ interaction on average. There is no surprise, though, as a specific case does not correspond to the average. As shown in Figure 3, the charge of N^* for the H-bond is only -0.92 to -0.96 e, while the charge of O for the H-bond is -1.21 e. Moreover, the H-bond distance of $OH \cdots N$ is larger than that of $OH \cdots O$. Consequently, the $OH \cdots N$ H-bond here is weaker and less effective in reducing the activation energy than the $OH \cdots O$ H-bond. Nevertheless, it is interesting to see the relatively weak $OH \cdots N$ H-bond is very effective in maintaining the charge of H in the reaction path that the O–H bond is stretched from the initial 0.98 Å to 1.51 Å at the transition state. Overall, a near constant charge of H during the O–H scission process as maintained by the H-bond interaction is a common feature for the H-bond catalyzed reactions. The effectiveness of an H-bond on lowering the activation energy is, however, dependent on numerous factors, such as the H-bond strength, the O–H bond strength, and the surface material, and thus requires further studies.

4. Conclusions

Oxhydryl dehydrogenations of H_xCOH^* ($x = 3, 2, 1, 0$) on Ni(111) were investigated by DFT calculations and Bader charge analysis. The activation energies are 68 to 91 kJ/mol for isolated H_xCOH^* and much reduced to 12–17 kJ/mol if assisted by neighboring OH^* . The catalyzing effect of OH^* is attributed to the $OH \cdots O$ H-bond that maintains the charge of oxhydryl H in the O–H bond breaking process. The catalytic mechanism of H-bond is further supported by the results of OH^* and N^* assisted dehydrogenation of OH^* . Due to the universality of H-bond, the catalytic mechanics revealed here are of broad implication to the study of reaction kinetics of many systems.

Author Contributions: Funding acquisition, Z.L.; Investigation, C.K.; Methodology, C.K.; Resources, Z.L.; Software, Z.L.; Supervision, Z.L.; Writing, C.K. and Z.L. All authors have read and agreed to the published version of the manuscript.

Funding: This research was funded by National Natural Science Foundation of China (11774324 & 11574284).

Acknowledgments: The computing time of the Super-computing Center of the University of Science and Technology of China are gratefully acknowledged.

Conflicts of Interest: The authors declare no conflict of interest.

References

1. Herdem, M.S.; Sinaki, M.Y.; Farhad, S.; Hamdullahpur, F. An overview of the methanol reforming process: Comparison of fuels, catalysts, reformers, and systems. *Int. J. Energy Res.* **2019**, *43*, 5076–5105. [[CrossRef](#)]
2. Khzouz, M.; Gkanas, E.I.; Du, S.; Wood, J. Catalytic performance of Ni-Cu/Al₂O₃ for effective syngas production by methanol steam reforming. *Fuel* **2018**, *232*, 672–683. [[CrossRef](#)]
3. Papavasiliou, J.; Paxinou, A.; Słowik, G.; Neophytides, S.; Avgouropoulos, G. Steam reforming of methanol over nanostructured Pt/TiO₂ and Pt/CeO₂ catalysts for fuel cell applications. *Catalysts* **2018**, *8*, 544. [[CrossRef](#)]
4. Trimm, D.L.; Önsan, Z.I. Onboard fuel conversion for hydrogen-fuel-cell-driven vehicles. *Catal. Rev.* **2001**, *43*, 31–84. [[CrossRef](#)]
5. Liu, Z.; Yao, S.; Johnston-Peck, A.; Xu, W.; Rodriguez, J.A.; Senanayake, S.D. Methanol steam reforming over Ni-CeO₂ model and powder catalysts: Pathways to high stability and selectivity for H₂/CO₂ production. *Catal. Today* **2018**, *311*, 74–80. [[CrossRef](#)]
6. Lu, J.; Li, X.; He, S.; Han, C.; Wan, G.; Lei, Y.; Chen, R.; Liu, P.; Chen, K.; Zhang, L.; et al. Hydrogen production via methanol steam reforming over Ni-based catalysts: Influences of Lanthanum (La) addition and supports. *Int. J. Hydrogen Energy* **2017**, *42*, 3647–3657. [[CrossRef](#)]

7. Kaftan, A.; Kusche, M.; Laurin, M.; Wasserscheid, P.; Libuda, J. KOH-promoted Pt/Al₂O₃ catalysts for water gas shift and methanol steam reforming: An operando DRIFTS-MS study. *Appl. Catal. B* **2017**, *201*, 169–181. [[CrossRef](#)]
8. Lin, S.; Xie, D.; Guo, H. Methyl formate pathway in methanol steam reforming on copper: Density functional calculations. *ACS Catalysis* **2011**, *1*, 1263–1271. [[CrossRef](#)]
9. Zuo, Z.-J.; Wang, L.; Han, P.-D.; Huang, W. Insights into the reaction mechanisms of methanol decomposition, methanol oxidation and steam reforming of methanol on Cu(111): A density functional theory study. *Int. J. Hydrogen Energy* **2014**, *39*, 1664–1679. [[CrossRef](#)]
10. Wang, S.-S.; Su, H.-Y.; Gu, X.-K.; Li, W.-X. Differentiating intrinsic reactivity of Copper, Copper–Zinc Alloy, and Copper/Zinc Oxide interface for methanol steam reforming by first-principles theory. *J. Phys. Chem. C* **2017**, *121*, 21553–21559. [[CrossRef](#)]
11. Wang, S.-S.; Gu, X.-K.; Su, H.-Y.; Li, W.-X. First-principles and microkinetic simulation studies of the structure sensitivity of Cu catalyst for methanol steam reforming. *J. Phys. Chem. C* **2018**, *122*, 10811–10819. [[CrossRef](#)]
12. Smith, G.K.; Lin, S.; Lai, W.; Datye, A.; Xie, D.; Guo, H. Initial steps in methanol steam reforming on PdZn and ZnO surfaces: Density functional theory studies. *Surf. Sci.* **2011**, *605*, 750–759. [[CrossRef](#)]
13. Krajčí, M.; Tsai, A.P.; Hafner, J. Understanding the selectivity of methanol steam reforming on the (1 1 1) surfaces of NiZn, PdZn and PtZn: Insights from DFT. *J. Catal.* **2015**, *330*, 6–18. [[CrossRef](#)]
14. Chen, W.; Cubuk, E.D.; Montemore, M.M.; Reece, C.; Madix, R.J.; Friend, C.M.; Kaxiras, E. A comparative ab initio study of anhydrous dehydrogenation of linear-chain alcohols on Cu(110). *J. Phys. Chem. C* **2018**, *122*, 7806–7815. [[CrossRef](#)]
15. Lausche, A.C.; Abild-Pedersen, F.; Madix, R.J.; Nørskov, J.K.; Studt, F. Analysis of sulfur-induced selectivity changes for anhydrous methanol dehydrogenation on Ni(100) surfaces. *Surf. Sci.* **2013**, *613*, 58–62. [[CrossRef](#)]
16. Kramer, Z.C.; Gu, X.-K.; Zhou, D.D.Y.; Li, W.-X.; Skodje, R.T. Following molecules through reactive networks: Surface catalyzed decomposition of methanol on Pd(111), Pt(111), and Ni(111). *J. Phys. Chem. C* **2014**, *118*, 12364–12383. [[CrossRef](#)]
17. Du, P.; Wu, P.; Cai, C. Mechanism of methanol decomposition on the Pt₃Ni(111) surface: DFT study. *J. Phys. Chem. C* **2017**, *121*, 9348–9360. [[CrossRef](#)]
18. Liao, T.-W.; Yadav, A.; Ferrari, P.; Niu, Y.; Wei, X.-K.; Vernieres, J.; Hu, K.-J.; Heggen, M.; Dunin-Borkowski, R.E.; Palmer, R.E.; et al. Composition-tuned Pt-skinned PtNi bimetallic clusters as highly efficient methanol dehydrogenation catalysts. *Chem. Mater.* **2019**, *31*, 10040–10048. [[CrossRef](#)]
19. Luo, W.; Asthagiri, A. Density functional theory study of methanol steam reforming on Co(0001) and Co(111) surfaces. *J. Phys. Chem. C* **2014**, *118*, 15274–15285. [[CrossRef](#)]
20. Kim, D.K.; Iglesia, E. Isotopic and kinetic assessment of the mechanism of CH₃OH-H₂O catalysis on supported Copper clusters. *J. Phys. Chem. C* **2008**, *112*, 17235–17243. [[CrossRef](#)]
21. Lee, J.K.; Ko, J.B.; Kim, D.H. Methanol steam reforming over Cu/ZnO/Al₂O₃ catalyst: Kinetics and effectiveness factor. *Appl. Catal., A* **2004**, *278*, 25–35. [[CrossRef](#)]
22. Blaylock, D.W.; Zhu, Y.-A.; Green, W.H. Computational investigation of the thermochemistry and kinetics of steam methane reforming over a multi-faceted nickel catalyst. *Top. Catal.* **2011**, 828–844. [[CrossRef](#)]
23. Kresse, G.; Furthmüller, J. Efficient iterative schemes for ab initio total-energy calculations using a plane-wave basis set. *Phys. Rev. B* **1996**, *54*, 11169–11186. [[CrossRef](#)] [[PubMed](#)]
24. Kresse, G.; Furthmüller, J. Efficiency of ab-initio total energy calculations for metals and semiconductors using a plane-wave basis set. *Comput. Mater. Sci.* **1996**, *6*, 15–50. [[CrossRef](#)]
25. Kresse, G.; Hafner, J. Ab initio molecular dynamics for liquid metals. *Phys. Rev. B* **1993**, *47*, 558–561. [[CrossRef](#)]
26. Kresse, G.; Hafner, J. Ab initio molecular-dynamics simulation of the liquid-metal-amorphous-semiconductor transition in germanium. *Phys. Rev. B* **1994**, *49*, 14251–14269. [[CrossRef](#)]
27. Kresse, G.; Joubert, D. From ultrasoft pseudopotentials to the projector augmented-wave method. *Phys. Rev. B* **1999**, *59*, 1758–1775. [[CrossRef](#)]
28. Blochl, P.E. Projector augmented-wave method. *Phys. Rev. B* **1994**, *50*, 17953–17979. [[CrossRef](#)]
29. Klimes, J.; Bowler, D.R.; Michaelides, A. Chemical accuracy for the van der Waals density functional. *J. Phys. Condens. Matter* **2010**, *22*, 022201. [[CrossRef](#)]
30. Klimes, J.; Bowler, D.R.; Michaelides, A. Van der Waals density functionals applied to solids. *Phys. Rev. B* **2011**, *83*. [[CrossRef](#)]

31. Carrasco, J.; Klimes, J.; Michaelides, A. The role of van der Waals forces in water adsorption on metals. *J. Chem. Phys.* **2013**, *138*, 024708. [[CrossRef](#)] [[PubMed](#)]
32. Press, W.H.; Flannery, B.P.; Teukolsky, S.A.; Vetterling, W.T. *Numerical Recipes: The Art of Scientific Computing*; Cambridge University Press: Cambridge, UK, 1986.
33. Henkelman, G.; Jonsson, H. Improved tangent estimate in the nudged elastic band method for finding minimum energy paths and saddle points. *J. Chem. Phys.* **2000**, *113*, 9978–9985. [[CrossRef](#)]
34. Henkelman, G.; Jonsson, H. A dimer method for finding saddle points on high dimensional potential surfaces using only first derivatives. *J. Chem. Phys.* **1999**, *111*, 7010–7022. [[CrossRef](#)]
35. Sanville, E.; Kenny, S.D.; Smith, R.; Henkelman, G. Improved grid-based algorithm for Bader charge allocation. *J. Comput. Chem.* **2007**, *28*, 899–908. [[CrossRef](#)]
36. Tang, W.; Sanville, E.; Henkelman, G. A grid-based Bader analysis algorithm without lattice bias. *J. Phys. Condens. Matter* **2009**, *21*, 084204. [[CrossRef](#)]
37. Wang, G.C.; Zhou, Y.H.; Morikawa, Y.; Nakamura, J.; Cai, Z.S.; Zhao, X.Z. Kinetic mechanism of methanol decomposition on Ni(111) surface: A theoretical study. *J. Phys. Chem. B* **2005**, *109*, 12431–12442. [[CrossRef](#)]
38. Zhou, Y.-H.; Lv, P.-H.; Wang, G.-C. DFT studies of methanol decomposition on Ni(100) surface: Compared with Ni(111) surface. *J. Mol. Catal. A Chem.* **2006**, *258*, 203–215. [[CrossRef](#)]
39. Greeley, J.; Mavrikakis, M. Methanol decomposition on Cu(111): A DFT study. *J. Catal.* **2002**, *208*, 291–300. [[CrossRef](#)]
40. Huang, Y.; He, X.; Chen, Z.X. Density functional study of methanol decomposition on clean and O or OH adsorbed PdZn(111). *J. Chem. Phys.* **2013**, *138*, 184701. [[CrossRef](#)]
41. Ke, C.; Lin, Z. Density functional theory based micro- and macro-kinetic studies of Ni-catalyzed methanol steam reforming. *Catalysts* **2020**, *10*, 349. [[CrossRef](#)]
42. Ke, C.; Lin, Z. Elementary reaction pathway study and a deduced macrokinetic model for the unified understanding of Ni-catalyzed steam methane reforming. *React. Chem. Eng.* **2020**. [[CrossRef](#)]
43. Che, F.L.; Gray, J.T.; Ha, S.; McEwen, J.S. Catalytic water dehydrogenation and formation on nickel: Dual path mechanism in high electric fields. *J. Catal.* **2015**, *332*, 187–200. [[CrossRef](#)]

Sample Availability: Samples of the compounds are available from the authors.



© 2020 by the authors. Licensee MDPI, Basel, Switzerland. This article is an open access article distributed under the terms and conditions of the Creative Commons Attribution (CC BY) license (<http://creativecommons.org/licenses/by/4.0/>).